Mathematical problems in mechanics/Calculus of variations

Optimization of the branching pattern in coherent phase transitions

Optimisation d'un motif de ramification au cours de la transformation de phase martensitique

Patrick Dondl [a], Behrend Heeren [b], Martin Rumpf [b]

[a] *Abteilung für Angewandte Mathematik, Albert-Ludwigs-Universität Freiburg, Hermann-Herder-Str. 10, 79104 Freiburg im Breisgau, Germany*
[b] *Institute for Numerical Simulation, Bonn University, Endenicher Allee 60, 53115 Bonn, Germany*

A R T I C L E   I N F O

A B S T R A C T

Branching can be observed at the austenite–martensite interface of martensitic phase transformations. For a model problem, Kohn and Müller studied a branching pattern with optimal scaling of the energy with respect to its parameters. Here, we present finite element simulations that suggest a topologically different class of branching patterns and derive a novel, low-dimensional family of patterns. After a geometric optimization within this family, the resulting pattern bears a striking resemblance to our simulation. The novel microstructure admits the same scaling exponents, but results in a significantly lower upper energy bound.

© 2016 Académie des sciences. Published by Elsevier Masson SAS. All rights reserved.

R É S U M É

Un motif de ramification est observé à l'interface austénite–martensite au cours de la transformation de phase martensitique. Kohn et Müller étudient un motif de ramification qui reflète les exposants optimaux de l'énergie en fonction de ses paramètres. Nous présentons ici des simulations par la méthode des éléments finis qui suggèrent une classe de ramifications ayant une topologie différente, et déduisons une nouvelle famille de ramifications, de faibles dimensions. Après optimisation géométrique au sein de cette famille, le motif résultant présente une ressemblance remarquable avec les résultats de notre simulation. Le nouveau motif possède les mêmes exposants d'échelle optimaux, mais fournit une constante significativement inférieure dans le contrôle de l'énergie.

© 2016 Académie des sciences. Published by Elsevier Masson SAS. All rights reserved.

E-mail addresses: patrick.dondl@mathematik.uni-freiburg.de (P. Dondl), behrend.heeren@ins.uni-bonn.de (B. Heeren), martin.rumpf@ins.uni-bonn.de (M. Rumpf).
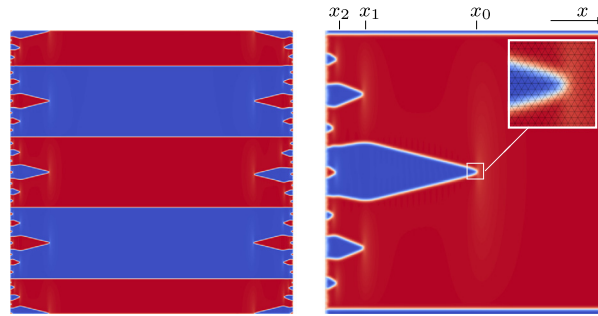
Fig. 1. Different zooms are displayed for a discrete minimizer of the energy $E_{\tilde{\epsilon}}$ in (2) with 10^6 elements on $\Omega = [0, 1]^2$ with $\tilde{\epsilon} = 2\sqrt{5} \cdot 10^{-3}$ and $\sigma = 10$, where blue encodes $u_y \approx -1$ and red $u_y \approx +1$.

1. Introduction

In this article, we study a non-convex scalar variational problem [7,12,1,8] considered to be a model for austenite–martensite interfaces in solid–solid phase transitions. Such interfaces often exhibit characteristic fine-scale phase mixtures, where the austenite phase, of higher crystallographic symmetry, is separated from thin layers of alternating martensitic phase variants. In the seminal work by Kohn and Müller [8,9], the energy functional

$$F_\epsilon[u] = \int_\Omega \epsilon \, |u_{yy}| + u_x^2 \; dx \, dy \tag{1}$$

was studied for suitable $u\colon \Omega \to \mathbb{R}$ with $\Omega = (0, L) \times (0, 1) \subset \mathbb{R}^2$ under the constraint that $u_y = \pm 1$ almost everywhere and $u = 0$ on $\partial\Omega$. They show that there are constants $c, C > 0$ such that $c\,\epsilon^{2/3} L^{1/3} \leq \min F_\epsilon[u] \leq C\,\epsilon^{2/3} L^{1/3}$. In order to recover the upper bound, they use an explicitly constructed branching pattern, which – after some optimization – yields a constant $C = 6.86$. In [4], Conti proved the asymptotic self-similarity of the energy minimizer near the Dirichlet boundary at $x = 0$, in the sense that the sequence $u_j(x, y) = \theta^{-2j/3} u(\theta^j x, \theta^{2j/3} y)$ admits a $W^{1,2}$-strongly converging subsequence. A corresponding diffuse interface Landau-type energy functional approximating F_ϵ is given by

$$E_{\tilde{\epsilon}}[u] = \int_\Omega \tfrac{1}{2}\,\tilde{\epsilon}^2\,u_{yy}^2 + \sigma\,(u_y^2 - 1)^2 + u_x^2 \; dx \, dy, \tag{2}$$

with given $\sigma > 0$, which corresponds to an effective interfacial energy of $\epsilon = \frac{2\sqrt{2\sigma}}{3}\tilde{\epsilon}$ in (1), cf. eq. (1.3) in [9]. Here, we report on a high-precision subdivision finite element simulation of this diffuse model, which allowed us to observe a particular branching pattern, which differs substantially from the construction studied in [8] as well as from other proposed patterns [10]. Based on this insight from the numerical experiment, we construct a novel, low-dimensional family of branching microstructures for the sharp-interface model (1). Optimizing over all geometric degrees of freedom in our model, the resulting pattern shows a striking geometric resemblance of the subdivision finite element simulation results. Furthermore, our branching pattern yields a significantly lower upper bound constant C for the energy.

2. Optimal branching pattern observed via FEM simulation for diffuse interfaces

The branching pattern investigated in this paper is derived from the results of a finite element simulation of the diffuse interface model. To minimize the energy (2) via a conforming finite element method, H^2-regular ansatz functions have to be taken into account. To this end, we fix $L = 1$ and use a conforming subdivision finite element approach [2,3,5] with C^2 basis functions that are quartic polynomials defined via Loop subdivision on a regular triangular mesh on the domain $\Omega = (0, L) \times (0, 1)$. We consider zero Dirichlet boundary conditions. To compute a discrete minimizer, we consider a discrete gradient flow approach combined with a convex–concave splitting proposed by D. Eyre [6] for the Cahn–Hilliard equation, which turns out to be unconditionally stable. By this method, the branching pattern can robustly be computed independently of the chosen initial data. Fig. 1 depicts the numerically computed minimizer of the energy (2). Obviously, branching starts at $x = x_0$ with the generation of one horizontal needle (blue). We denote the vertical stripe between $x = x_0$ and $x = x_1$ as the first *branching layer*. The second branching layer is located between $x = x_1$ and $x = x_2$, where two new needles (blue) are generated, one on either side of the needle from the previous layer. Then in the third branching layer (starting at $x = x_2$) four new needles (blue) are generated, i.e. one on either side of the two blue needles from the previous layer and, additionally, one (red) needle in the interior of the needle that was generated in the last but one layer. Hence, the pattern is topologically different from the one investigated by Kohn and Müller [8], where interior needles are not present. Furthermore, the pattern in our simulations differs geometrically from that proposed by Li [10], where *interior* needles are generated in every layer, whereas in our pattern they arise *every other* layer. Let us mention that a topologically equivalent,
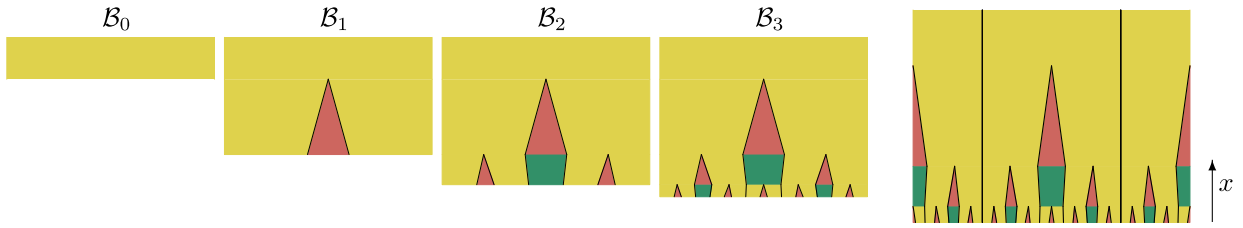
Fig. 2. Constructing a periodic cell $\mathcal{P}_3$ with $K = 3$ levels. Starting from the initial word $\mathcal{B}_0 = \omega_0 = f$, the automaton is applied three times to construct $\mathcal{B}_1, \mathcal{B}_2, \mathcal{B}_3$ (using the (NEW) scheme). Afterwards, a y-periodic cell $\mathcal{P}_3$ is constructed by reflecting half of the pattern $\mathcal{B}_3$ to either side along two straight additional interfaces (right). Color code: facet (yellow), spike (red) and trunk (green); black lines denote interfaces separating regions with $u_y = \pm 1$. All patterns $\mathcal{B}_k$ and $\mathcal{P}_3$ have been rotated by 90° for better visualization. Note: The color coding does *not* represent different phases of martensite (as in Fig. 3).
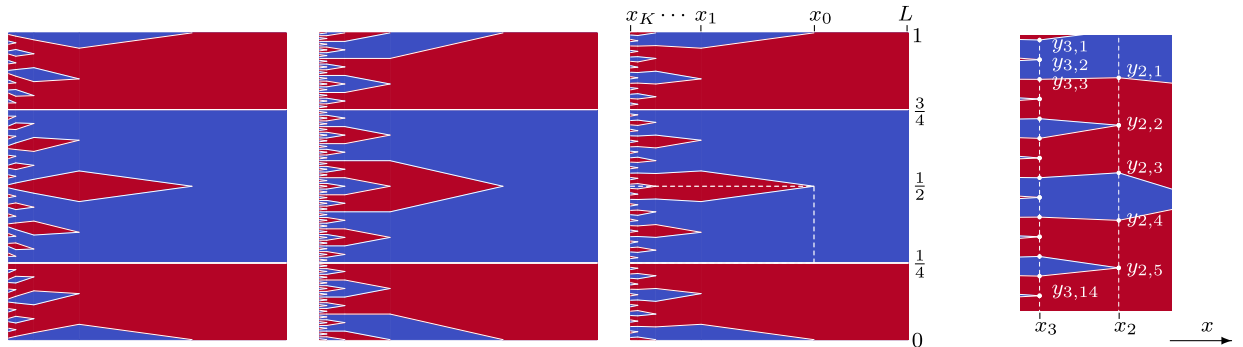
Fig. 3. Periodic cell $\mathcal{P}_4$ for (KM), (L) and (NEW) from left to right, with $x_k = \theta^k l$ for $k \geq 0$ and $l < L$. Here the color encodes the sign of u_y. The computational domain $\mathcal{C}_K = [x_K, x_0] \times [\frac{1}{4}, \frac{1}{2}]$ is surrounded by the dotted line in the (NEW) scheme. By construction, the pattern is symmetric along $y = \frac{1}{2}$, ensuring periodic boundary conditions, i.e. $u(x, 0) = u(x, 1)$. Degrees of freedom in y-direction are shown on the right (white dots), i.e. $y_{k,n}$ for $n = 1, \ldots, n_k$ for each level k.

however geometrically somewhat distorted pattern has been found in less accurate simulations by Muite [11]. Swart and Holmes [13] also observed a very similar branching pattern as steady state in their simulations of the dynamic problem with inertia and damping, but without an explicit surface energy.

3. Optimal branching pattern for a reduced sharp-interface model

Now, we will use the findings for the diffuse interface model from the previous section to derive a geometrically simple, reduced model for the sharp-interface problem (1), optimize over its degrees of freedom, and compare it in terms of the stored energy with the correspondingly optimized version of the pattern proposed by Kohn, Müller and by Li.

Topology. For the reduced model, we restrict the ansatz space for u via an assumption on the geometry of the interfaces where the gradient of u jumps. In fact, we suppose this interface set to consist of piecewise polygonal lines separating regions with $u_y = \pm 1$. The branching pattern is now constructed by defining needles of different sizes, which are bounded by these polygonal lines. We assume that one needle consists of a trunk (t) and a spike (s) on top of it, the material outside a needle is referred to as a facet (f). The generation of a particular branching pattern is described best by the action of an *automaton* $\mathcal{A}$. We consider the alphabet $\{f, s, t, |\}$, where $|$ denotes an interface. The initial word is given by $\omega_0 = f$. A branching pattern after K iterations is defined by $\mathcal{B}_K = \omega_0; \mathcal{A}(\omega_0); \ldots; \mathcal{A}^K(\omega_0)$, where ; represents the generation of a new level. The action of $\mathcal{A}$ on a word is realized letter by letter where $\mathcal{A}(|) = |$ for all patterns. Different branching patterns are characterized by the action of $\mathcal{A}$ on the three letters $\{f, s, t\}$. The new branching pattern (NEW) described in Section 2 is characterized by $\mathcal{A}(s) = t$ and $\mathcal{A}(t) = \mathcal{A}(f) = f \,|\, s \,|\, f$ (cf. Fig. 2). The pattern investigated by Kohn and Müller [8] (KM) is generated by the rules $\mathcal{A}(s) = t$, $\mathcal{A}(t) = t$ and $\mathcal{A}(f) = f \,|\, s \,|\, f$, and the pattern proposed by Li [10] (L) is given by the rules $\mathcal{A}(s) = \mathcal{A}(f) = f \,|\, s \,|\, f$. There are no trunks t in the Li model. A periodic cell $\mathcal{P}_K$ with K levels is now defined by computing $\mathcal{B}_K$ (as described above) and then reflecting half of the pattern to either side along two straight additional interfaces (as shown in Fig. 2, right). The constructed pattern consists of connected components (bounded by polygonal lines), which will later represent different phases of martensite, i.e. regions with $u_y = \pm 1$ (cf. Fig. 2 vs. 3).

Geometry. Now we describe the geometric arrangement of $\Omega = [0, L] \times [0, 1]$ (cf. Fig. 3). At first we assume that the geometry of the period cell $\mathcal{P}_K$ is fitted in y-direction to the interval $[0, 1]$. There is a region without any branching needles between $x = x_0 = l$ and $x = L$, corresponding to $\mathcal{B}_0$ in Fig. 2. Here, $l \in (0, L)$ is a degree of freedom. The kth branching level

(whose topology is described by the kth iteration of the automaton) is defined as the vertical stripe between $x = x_k = \theta^k l$ and $x = x_{k-1} = \theta^{k-1} l$, for $k = 1, \ldots, K$, where the scaling parameter $\theta \in (0, 1)$ is another degree of freedom. Note that all needles generated by the automaton are bounded by piecewise linear facets whose vertices $y_{k,n}$ are located by definition along vertical lines $x = x_k$ for each k (cf. Fig. 3, right). Hence, the geometric degrees of freedom in x-direction are given by θ and l, and in y-direction by the y-positions of the vertices $y_{k,n}$. Finally, we introduce a boundary layer (neither shown in Fig. 2 nor in Fig. 3) between $x = 0$ and $x = x_K$ in order to interpolate from the zero boundary conditions at $x = 0$ to the finest resolved branching level $\mathcal{B}_K$. In this boundary layer, we do no explicitly resolve the branching pattern anymore, but instead use an energy estimate as given in (6) below. By construction, the pattern is symmetric along $y = \frac{1}{2}$, ensuring periodic boundary conditions, i.e. $u(x, 0) = u(x, 1)$. We choose constant zero boundary conditions $u(x, 0) = u(x, 1) = 0$ which directly implies $u(x, \frac{1}{2}) = 0$, i.e. $u_x(x, \frac{1}{2}) = 0$. We assume that the tip of an (initial) needle and the tip of all needles being generated *within* this initial needle lie on a horizontal line. Note that this only applies to (NEW) and (L) as (KM) never produces new needles *within* one existing needle. Later, we will allow N repetitions of the periodic cell $\mathcal{P}_K$ in the y-direction, where $N \in \mathbb{N}$ is another degree of freedom.

Elastic energy. The computational domain $\mathcal{C}_K \subset \mathcal{P}_K$ is limited to $\mathcal{C}_K = [\theta^K l, l] \times [\frac{1}{4}, \frac{1}{2}]$, as indicated by the dotted lines in Fig. 3. The geometry of $\mathcal{C}_K$ is described by θ and the y coordinates of the interior vertices of the polygonal interfaces. We denote the vertices on the line with $x_k = \theta^k l$ from top to bottom by $y_{k,n}$ for $n = 1, \ldots n_k$ (cf. Fig. 3, right) and the open sets of constant slope u_y between the lines $x_{k-1} = \theta^{k-1} l$ and $x_k = \theta^k l$ by $\mathcal{R}_{k,i}$ for $i = 1, \ldots i_k$. As u is a piecewise linear function by construction, u_x is constant on the regions $\mathcal{R}_{k,i}$ for all i, k. Since $u_x(x, \frac{1}{2}) = 0$, we have $u_x|_{\mathcal{R}_{k,0}} = 0$. For $[y_{k-1,\overline{n}(k,i)}, y_{k,\underline{n}(k,i)}]$ being the upper edge of $\mathcal{R}_{k,i}$, the piecewise constant quantity u_x on the stripe $\mathcal{C}_K \cap \{x_k \leq x \leq x_{k-1}\}$ is described iteratively by

$$u_x|_{\mathcal{R}_{k,i+1}} = u_x|_{\mathcal{R}_{k,i}} + 2 \operatorname{sign}\left(u_y|_{\mathcal{R}_{k,i}}\right) \frac{y_{k-1,\overline{n}(k,i)} - y_{k,\underline{n}(k,i)}}{\theta^{k-1} l - \theta^k l}, \quad i \geq 0. \tag{3}$$

The elastic energy $\int_{\mathcal{C}_K} u_x^2 \, dx \, dy$ is given by $F_{\text{elast}}[\mathcal{C}_K] = \sum_{k=1}^K \sum_{i>0} (u_x|_{\mathcal{R}_{k,i}})^2 \cdot |\mathcal{R}_{k,i}|$. Due to the symmetry of $\mathcal{P}_K$, we have $F_{\text{elast}}[\mathcal{P}_K] = 4 F_{\text{elast}}[\mathcal{C}_K]$. Note that there is no contribution to the elastic energy in the stripe $\{(x, y) : l < x < L\}$. If we now rescale $\mathcal{P}_K$ in y-direction by N^{-1} (to allow N repetitions of $\mathcal{P}_K$), we have $u_x \sim N^{-1}$ and $|\mathcal{R}_{k,i}| \sim N^{-1}$. The total elastic energy F_{elast}^K is now given by summing over all N repetitions of $\mathcal{P}_K$, i.e. if we collect all $y_{k,i}$ in a vector $\mathbf{Y}$, we have

$$F_{\text{elast}}^K[\theta, N, l, \mathbf{Y}] = \int_{x > x_K} u_x^2 \, dx \, dy = 4 N^{-2} \sum_{k=1}^K \sum_{i>0} \left(u_x|_{\mathcal{R}_{k,i}}\right)^2 \cdot |\mathcal{R}_{k,i}| \quad \sim \quad c_{\text{elast}}(\theta, \mathbf{Y}) \, l^{-1} N^{-2}. \tag{4}$$

Surface energy. Let I_k denote the number of interfaces in $\mathcal{S}_k = \{(x, y) : x_k < x < x_{k-1}\} \subset \mathcal{P}_K$. Then we obtain $\int_{\mathcal{S}_k} \epsilon |u_{yy}| \, dx \, dy = 2\epsilon (x_{k-1} - x_k) I_k = 2\epsilon (1 - \theta)\theta^{k-1} l I_k$ for the interface energy which does not depend on the inner vertices $y_{k,i}$. Obviously $I_k = 2 \cdot (1 + 2\sum_{i=1}^k s_i)$, where s_i denotes the number of spikes in $\mathcal{S}_i$ between two parallel interfaces shown as vertical black lines in Fig. 2 (right). We deduce $s_i = 2^{i-1}$ for (KM) and $s_i = 3^{i-1}$ for (L), whereas for (NEW) the recursive relation $s_1 = 1$, $s_2 = 2$ and $s_i = 2 s_{i-1} + s_{i-2}$ for $i > 2$ implies $s_i = (\alpha - \beta)^{-1}(\alpha^i - \beta^i)$, where $\alpha = 1 + \sqrt{2}$ and $\beta = 1 - \sqrt{2}$. Plugging this into the formula for I_k yields $I_k = \alpha^{k+1} + \beta^{k+1}$ for (NEW), $I_k = 2(2^{k+1} - 1)$ for (KM) and $I_k = 2 \cdot 3^k$ for (L). If we take into account the two interfaces in $\{(x, y) \in \mathcal{P}_K : l < x < L\}$ and consider N repetitions of a rescaled cell $\mathcal{P}_K$, we get:

$$F_{\text{surf}}^{K,\epsilon}[\theta, N, l] = \int_{x > x_K} \epsilon |u_{yy}| \, dx \, dy = 2\epsilon N(1 - \theta) l \sum_{k=1}^K \theta^{k-1} I_k + 4\epsilon N(L - l) \quad \sim \quad c_{\text{surf}}(\theta) \, \epsilon \, l \, N. \tag{5}$$

Boundary conditions. So far we have neglected the energy in the domain $\Omega_\partial^K = \{(x, y) : 0 \leq x < x_K\}$. In particular, we have not specified how to fulfill the boundary conditions $u = 0$ at $x = 0$ in the reduced model. As there is no closed-form formula for the elastic energy on a stripe $\mathcal{S}_k$, we can evaluate (4) only for finite K. Similar to the proof of Lemma 2.3 in [4], we construct $\tilde{u} : \Omega_\partial^K \to \mathbb{R}$ explicitly, with $|\tilde{u}_y| = 1$, $\tilde{u}(0, y) = 0$ and $\tilde{u}(x_K, y) = u(x_k, y)$, and estimate the elastic energy in Ω_∂^K by $\int_{\Omega_\partial^K} \tilde{u}_x^2 \, dx \, dy$. Furthermore, we will ensure that $\int_{\Omega_\partial^K} \epsilon |\tilde{u}_{yy}| \, dx \, dy = \int_{\Omega_\partial^K} \epsilon |u_{yy}| \, dx \, dy = 2\epsilon N(1 - \theta) l \sum_{k>K} \theta^{k-1} I_k$, cf. (5). The sum on the right-hand side converges if $\alpha\theta < 1$ for (NEW), $2\theta < 1$ for (KM) and $3\theta < 1$ for (L) and the limit can be computed explicitly. Hence we get a remaining energy

$$\int_{\Omega_\partial^K} \epsilon |u_{yy}| + u_x^2 \, dx \, dy \leq \frac{c_{\text{rem}}(\theta)}{\theta^K l N^2} + \frac{\|u(x_K, \cdot)\|_{L^2(0,1)}^2}{\theta^K l} + 2\epsilon N(1 - \theta) l \sum_{k>K} \theta^{k-1} I_k =: F_\partial^{K,\epsilon}[\theta, N, l, (y_{K,i})_i]. \tag{6}$$

Note that $\|u(x_K, \cdot)\|^2$ depends on $(y_{K,i})_i$ and scales like N^{-2}. Furthermore the constant $c_{\text{rem}}(\theta)$ is the limit of a geometric series that converges if $\alpha^2 \theta > 1$ for (NEW), $4\theta > 1$ for (KM) and $9\theta > 1$ for (L).

	$F^{K,\epsilon}$	$F_\partial^{K,\epsilon}$	l	θ
NEW	0.2113	$5.1 \cdot 10^{-4}$	0.146	0.273
L	0.2140	$2.9 \cdot 10^{-4}$	0.158	0.198
KM	0.2371	$1.3 \cdot 10^{-2}$	0.119	0.366

Fig. 4. Optimal values for NEW ($K = 17$), L ($K = 14$) and KM ($K = 12$) for fixed $N = 2$.
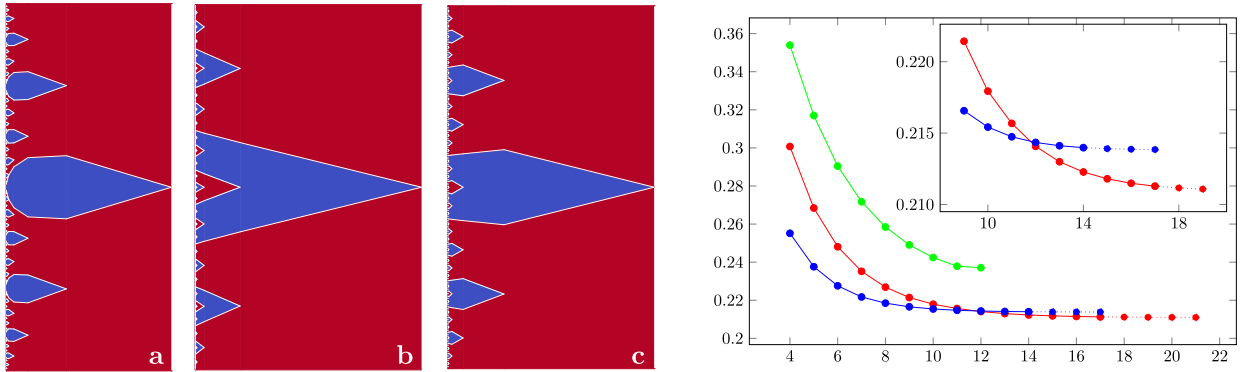

Fig. 5. From left to right: optimal patterns of the reduced model (with $\epsilon = 0.013$ and fixed $N = 2$) for (KM) with $K = 12$, (L) with $K = 14$ and (NEW) with $K = 17$, restricted to the domain $[\theta^K l, l] \times [3/8, 5/8]$. Right: optimal energy for (NEW) in red, (L) in blue and (KM) in green, with enlargements of crucial details. Dotted lines are extrapolations without optimization, nevertheless, energies are monotonically decreasing. Numerical optimization breaks down for (KM) if $K > 12$ due to degeneration of geometry on high levels.

Optimization. Using (4), (5) and (6) we obtain the objective functional for $\epsilon > 0$ and $K \in \mathbb{N}$

$$F^{K,\epsilon}[\theta, N, l, \mathbf{Y}] = F_{\text{elast}}^K[\theta, N, l, \mathbf{Y}] + F_{\text{surf}}^{K,\epsilon}[\theta, N, l] + F_\partial^{K,\epsilon}[\theta, N, l, (y_{K,i})_i]. \tag{7}$$

Optimizing $F^{K,\epsilon}$ for N yields $N \sim \epsilon^{-1/3} l^{-2/3}$, i.e. we get the expected scaling $F^{K,\epsilon} \sim \epsilon^{2/3} l^{1/3}$.

We now optimize $F^{K,\epsilon}$ in (7) with respect to θ, l, $\mathbf{Y}$ for fixed $\epsilon > 0$, $L = 0.5$ and $K \in \mathbb{N}$ for the three different reduced models (L), (KM), and (NEW). One may also consider $N \in \mathbb{N}$ as an additional degree of freedom, which is realized by assuming $N \in \mathbb{R}$ in the simulations. In order to compare the results to the finite element simulation of the diffuse interface model shown in Fig. 1, where $\tilde{\epsilon} = 2\sqrt{5} \cdot 10^{-3}$ and $\sigma = 10$ we set $\epsilon = \frac{2\sqrt{2\sigma}}{3}\tilde{\epsilon} \approx 0.013$ in the reduced model; cf. eq. (1.3) in [9].

The simulation is initialized on level $K = 4$ with the patterns shown in Fig. 3. After optimizing all degrees of freedom on this level, K is increased by one by extrapolating the solution of the last level and the whole pattern is optimized again. This procedure is repeated iteratively.

4. Discussion and comparison of the branching pattern

The optimal patterns of the reduced models (for fixed $N = 2$) are compared to each other in Fig. 5. First, the reduced (KM) pattern degenerates already at level $K = 13$, i.e. the monotonicity of the sequence $(y_{k,i})_i$ for $k \approx K$ is violated. In particular, it is energetically not competitive (cf. Figs. 4 and 5, right). Qualitatively, the optimal pattern of (NEW) in Fig. 5c is very similar to the optimal pattern of the diffuse interface model in Fig. 1. Striking is the fact that all needles of (NEW) are actually diamond-shaped, i.e. bounded by a polygon consisting of *four straight* lines. Up to some numerical perturbations (probably due to boundary effects), this can also be observed in the pattern in Fig. 1. However, these straight lines are not mandatory in the reduced model due to the freedom to move $y_{k,i}$. For instance, this is not the case for the optimal pattern of (L) and (KM), cf. Fig. 5a and 5b. The similarity between the optimal (NEW) pattern and the optimal pattern of the diffuse interface model also holds quantitatively. First, for (NEW) the optimal value $\theta = 0.273$ reflects very well the corresponding measured ratio $\theta \approx 0.26$ in Fig. 1. Second, the ratio "width-to-height" of the largest needle is approximately 2.6 in Fig. 1 and 2.7 for the optimal pattern of (NEW), Fig. 5c. Furthermore, this ratio decreases in both patterns almost equally when going to the second largest needle.

Among the reduced models, the (NEW) pattern performs best energetically, with a relative difference of $>1\%$ w.r.t. the optimal energy of (L), see Fig. 4. Although the difference is not particularly large, it is stable with respect to a variation of the model parameters ϵ, L and N (not shown here). In particular, this remains true when optimizing over all degrees of freedom (cf. Fig. 6). Fig. 6 further reveals that the difference $\Delta F^{K,\epsilon}$ of the optimal energies is of the order of 10^{-3}, whereas the error (due to the estimate (6) in the boundary layer Ω_∂) is of the order of 10^{-4}. Furthermore, the estimate (6) is not sharp and hence $F_\partial^{K,\epsilon}$ is dominant for small K, which leads to a substantial over-prediction of the energy of (NEW) for $K < 13$ (cf.

	$F^{K,\epsilon}$	$F_\partial^{K,\epsilon}$	N	l	θ
NEW	0.2073	$4.4 \cdot 10^{-4}$	2.661	0.095	0.273
L	0.2096	$2.5 \cdot 10^{-4}$	2.689	0.101	0.198

Fig. 6. Optimal values for NEW ($K = 17$) and L ($K = 14$) with free $N \in \mathbb{R}$. Note that $\Delta F^{K,\epsilon} \sim 10^{-3}$ whereas $F_\partial^{K,\epsilon} \sim 10^{-4}$.

Fig. 5, right). To compare the results to the upper constant $C = 6.86$, given in [8], we compute $C = \min(F^{K,\epsilon}) L^{-1/3} \epsilon^{-2/3}$ and get $C = 4.81$ ($N = 2$ fixed) or even $C = 4.72$ (free $N \in \mathbb{R}$) for (NEW) and $C = 4.87$ or $C = 4.78$ for (L), respectively.

Acknowledgements

References

[1] J. Ball, R.D. James, Fine phase mixtures as minimizers of the energy, Arch. Ration. Mech. Anal. 100 (1987) 13–52.
[2] Fehmi Cirak, Quan Long, Subdivision shells with exact boundary control and non-manifold geometry, Int. J. Numer. Methods Eng. 88 (9) (2011) 897–923.
[3] Fehmi Cirak, Michael Ortiz, Peter Schröder, Subdivision surfaces: a new paradigm for thin-shell finite-element analysis, Int. J. Numer. Methods Eng. 47 (12) (2000) 2039–2072.
[4] Sergio Conti, Branched microstructures: scaling and asymptotic self-similarity, Commun. Pure Appl. Math. 53 (2000) 1448–1474.
[5] Patrick W. Dondl, Ching-Ping Shen, Kaushik Bhattacharya, Computational analysis of martensitic thin films using subdivision surfaces, Int. J. Numer. Methods Eng. 72 (1) (2007) 72–94.
[6] David J. Eyre, Unconditionally gradient stable time marching the Cahn–Hilliard equation, Mater. Res. Soc. Symp. Proc. 529 (1998) 39–46.
[7] A.G. Khachaturyan, Theory of Structural Transformations in Solids, Wiley, New York, 1983.
[8] R.V. Kohn, S. Müller, Branching of twin near an austenite–twinned-martensite interface, Philos. Mag. A 66 (5) (1992) 697–715.
[9] R.V. Kohn, S. Müller, Surface energy and microstructure in coherent phase transitions, Commun. Pure Appl. Math. 47 (4) (1994) 405–435.
[10] Zhiping Li, Numerical justification of branched laminated microstructure with surface energy, SIAM J. Sci. Comput. 24 (3) (2003) 1054–1075.
[11] B.K. Muite, Analysis, modelling and simulation of shape memory alloys, PhD thesis, The Queen's College, University of Oxford, Oxford, UK, 2009.
[12] A.L. Roitburd, The domain structure of crystals formed in the solid phase, Sov. Phys., Solid State 10 (12) (1969) 2870–2876.
[13] Pieter J. Swart, Philip J. Holmes, Energy minimization and the formation of microstructure in dynamic anti-plane shear, Arch. Ration. Mech. Anal. 121 (1) (1992) 37–85.